JACS
JOURNAL OF THE AMERICAN CHEMICAL SOCIETY

ARTICLE

pubs.acs.org/JACS

Ligand-Passivated Eu:Y_2O_3 Nanocrystals as a Phosphor for White Light Emitting Diodes

Qilin Dai, Megan E. Foley, Christopher J. Breshike, Adrian Lita, and Geoffrey F. Strouse*

Department of Chemistry and Biochemistry, Florida State University, Tallahassee, Florida 32306-4390, United States

S *Supporting Information*

ABSTRACT: Eu(III)-doped Y_2O_3 nanocrystals are prepared by microwave synthetic methods as spherical 6.4 ± 1.5 nm nanocrystals with a cubic crystal structure. The surface of the nanocrystal is passivated by acetylacetonate (acac) and HDA on the Y exposed facet of the nanocrystal. The presence of acac on the nanocrystal surface gives rise to a strong $S_0 \rightarrow S_1$ ($\pi \rightarrow \pi^*$, acac) and acac → Ln^{3+} ligand to metal charge transfer (LMCT) transitions at 270 and 370 nm, respectively, in the Eu:Y_2O_3 nanocrystal. Excitation into the $S_0 \rightarrow S_1$ ($\pi \rightarrow \pi^*$) or acac → Ln^{3+} LMCT transition leads to the production of white light emission arising from efficient intramolecular energy transfer to the Y_2O_3 oxygen vacancies and the Eu(III) Judd−Ofelt f−f transitions. The acac passivant is thermally stable below 400 °C, and its presence is evidenced by UV−vis absorption, FT-IR, and NMR measurements. The presence of the low-lying acac levels allows UV LED pumping of the solid phosphor, leading to high quantum efficiency (∼19%) when pumped at 370 nm, high-quality white light color rendering (CIE coordinates 0.33 and 0.35), a high scotopic-to-photopic ratio (S/P = 2.21), and thermal stability. In a LED lighting package luminosities of 100 lm W^{-1} were obtained, which are competitive with current commercial lighting technology. The use of the passivant to funnel energy to the lanthanide emitter via a molecular antenna effect represents a new paradigm for designing phosphors for LED-pumped white light.

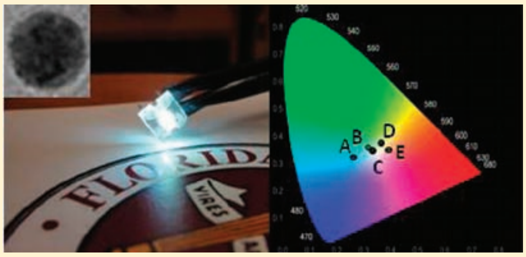

INTRODUCTION

The use of single-component white light phosphors pumped by high-efficiency UV LEDs, which operate in the wavelength range of 350−420 nm, represent a promising approach for low-cost, next-generation solid-state lighting, owing to their high efficiency in converting electrical energy to light, long duration and lifetime, good reliability and safety, easy maintenance, low energy consumption, and environmental advantages over currently employed mercury-based compact fluorescent lamps (CFLs).[1−7] High-efficiency LEDs pumping a phosphor are commonly employed in a variety of lighting applications from backlit LCD's to flashlights to, more recently, room lighting, as the luminous efficiency has increased from 5 to 150 lm W^{-1} for commercial LED based available solid-state lighting.[5−7] Many of these phosphors utilize blue LEDs (450−470 nm) to pump a YAG phosphor, which produces the characteristic blue/yellow color typical of modern LED flashlights. The blue color arises from the LED source, while the yellow is due to the downconversion YAG phosphor. The development of new white phosphors that exhibit lighting more characteristic of an incandescent source without the intense blue of the pumped LED is critical for applications in the household environment. Unfortunately, most phosphors have been optimized for 254 nm pumping in order to be used in compact fluorescent lighting (CFLs) and not the energies available for UV-LEDs (350−370 nm). While CFLs are already being utilized, the concern of Hg-based lighting and the potential cost savings due to lower energy usage and lower operating temperature of an LED-based lighting technology hold promise for LED-pumped white phosphor lighting technology.

The efficiency of LED-pumped phosphor-based lighting technology is directly dependent on the optical properties of the phosphors (optical cross section, radiative quantum yield) and the ability for the phosphor to nonradiatively downconvert excitation energy through energy transfer to the desired emissive state. To achieve more efficient LED-pumped phosphors, semiconductor quantum dots have been employed, due to their broad band excitation and size-dependent color,[8,9] as well as rare-earth (RE)-based phosphors in oxide, nitride, sulfide, and oxysulfide host lattices. The use of RE phosphors for lighting has gained attention, due to the reduced environmental toxicity concerns for RE phosphors;[10−12] however, RE phosphors in lanthanide sulfides are unstable toward degradation, RE phosphors in lanthanide nitrides lack cost-effective production methods, and RE phosphors in lanthanide oxysulfides have a poor optical cross section for excitation at energies lower than 300 nm.[13−15] Lanthanide oxide nanocrystals have been prepared in the literature by combustion, hydrothermal, and lyothermal methods but generally require long reaction times to produce dispersed nanocrystal powders.[16−26] The highest quality phosphors to date have been prepared by lyothermal techniques utilizing oleic acid as a ligand.[18] To realize the potential of white LEDs for solid-state lighting, the development of optimized phosphors that produce

Received: April 28, 2011
Published: August 24, 2011

dx.doi.org/10.1021/ja2039419 | *J. Am. Chem. Soc.* 2011, 133, 15475–15486

white light directly when pumped with commercial LEDs that operate between 350 and 420 nm is required. In addition, the LED-based lighting technology developed from the white phosphor must approach 100 lm W^{-1} to be competitive with current CFL technology.[7]

Rare-earth phosphors, in particular Eu:Y_2O_3 and derivatives of $Eu(acac)_3$, are well-known red downconversion phosphors used in commercial lighting and display technology, as well as recently in organic light emitting diodes (OLEDs).[27−36] These phosphors exhibit RE ion concentration dependent downconversion to the Eu(III) center by direct pumping of the $O_{2p} \rightarrow Eu_{4f}$ (III) charge transfer (CT) band and higher lying f−f levels at λ >250 nm; however, the phosphors cannot be efficiently pumped with commercial UV-LED sources which operate below 300 nm, due to the fact the low-lying f−f Judd−Ofelt (J-O) transitions for Eu^{3+} have small optical absorption cross sections. Various oxide hosts, as well as activator ion inclusion (Bi^{3+}, Zr^{4+}), have been investigated to improve the optical cross section for Eu(III) pumping, with limited success.[37−40] Research efforts have shown that nanoscale Eu:Y_2O_3 can shift and broaden the absorption band,[41] which can improve the direct excitation by UV-LEDs, but unfortunately the nanocrystals still lack a large spectral cross section in the appropriate spectral range for efficient pumping of the phosphor by a UV-LED.

In analogy to the photosynthetic reaction center,[42−46] one approach that has not attracted attention in the RE-doped oxide phosphor literature is the use of a passivating ligand on a nanocrystal as a molecular antenna for enhancing the optical cross section for absorption of the exciting LED energy. In RE diketonate complexes such as $Ln(acac)_3$ (Ln is a lanthanide ion), direct pumping of the diketonate ligand electronic levels leads to improved downconversion to the RE emitter via intramolecular energy transfer from the diketonate $S_0 \rightarrow S_1$ $\pi \rightarrow \pi^*$ transition or the low-energy ligand to metal charge transfer (LMCT) $O_{acac} \rightarrow$ Ln(III) transition at λ ~370 nm to the J-O levels of the RE ion.[47−57] The intramolecular energy transfer from the ligand to the lanthanide, which is often termed a molecular antenna effect, has been widely exploited in lanthanide coordination compounds, with the highest reported quantum efficiency for $Eu^{III}(tta)_3(DBSO)_2$ being $\phi_{em} \approx 85\%$.[56,58−60]

The use of a molecular antenna to improve the cross section for optical pumping of a nanophosphor by passivation of a Eu:Y_2O_3 nanocrystal by a diketonate ligand such as acetylacetonate (acac) should allow direct UV-LED pumping of the nanophosphor though improved intramolecular energy transfer to the Eu^{3+} RE emitter. In this paper, microwave (MW) reaction methods are employed to prepare 6.4 ± 1.5 nm spherical acac-passivated Eu(III)-doped Y_2O_3 nanocrystals. The concentration-dependent optical properties for acac−Eu:Y_2O_3 nanocrystals doped from 0% to 18% Eu(III) and phosphor efficiency are reported. The isolated nanocrystals from the MW method exhibit a cubic structure with evidence for ligand-induced face-specific faceting. The microwave-assisted reaction has several unique advantages over convective heating: namely, selective activation of the target precursor to initiate nucleation and subsequent growth, short reaction times, and reproducibility from batch to batch.[61−64] The Eu:Y_2O_3 nanocrystals are prepared in the 2.45 GHz MW cavity operating at 300 W in <15 min directly from the $Ln(acac)_3$ salts in hexadecylamine without the requirement of a cosolvent as previously reported.[18] Evidence for a thermally stable (below 400 °C) acac passivation layer on the Eu:Y_2O_3 nanocrystal is provided by FT-IR and ^{13}C solid-state NMR measurements.

The acac-passivated Eu:Y_2O_3 nanocrystals are observed to exhibit a strong $S_o \rightarrow S_1$ acac $\pi \rightarrow \pi^*$ transition at 270 nm and the LMCT $O_{acac} \rightarrow$ Ln(III) (Ln = Y, Eu) at 370 nm. The presence of the 370 nm $O_{acac} \rightarrow$ Ln(III) CT band is ideal for overlap with a UV-LED and is shown to produce white light with good color rendition (CIE coordinates of 0.33 and 0.35), high solid-state quantum efficiency for white light ($\phi_{em} \approx 19\%$), and high luminosity (100 lm W^{-1} at 3.3 V). The efficiency of the phosphor is concentration dependent. The white light exhibits a high S/P ratio (2.20), making the light source desirable for room-lighting applications.[65] The white light is generated from emission from a combination of localized Y_2O_3 oxygen defect levels and Eu(III) J-O transitions in the nanophosphor. The efficient production of white light from the acac-passivated Eu:Y_2O_3 nanophosphor implies that further tuning of the passivation ligand singlet and triplet levels can allow efficient UV-LED pumped phosphors to be designed that utilize ligand-based energy funneling via a molecular antenna effect for solid-state lighting applications.

EXPERIMENTAL SECTION

Synthesis of Eu:Y_2O_3 (0%, 2%, 9%, 11%, 18%) Nanocrystals. Eu:Y_2O_3 (nanocrystals passivated by 2,4-pentadione (acac) were prepared by microwave-induced decomposition of yttrium(III) 2,4-pentanedionate hydrate (Alfa Aesar, 99.9%) and europium(III) 2,4-pentanedionate hydrate (Alfa Aesar, 99.9%) in a CEM Discover Microwave (MW) operating under single mode, continuous power at 2.45 GHz. The CEM MW cavity was commercially modified by CEM with a Teflon insert to allow sustainable heating at 300 °C. A glass microwave reactor vessel containing yttrium(III) 2,4-pentanedionate hydrate (0.193 g, 0.5 mmol), europium(III) 2,4-pentanedionate hydrate (0% (0 g), 2% (0.0045 g), 9% (0.01125 g), 11% (0.0225 g), 18% (0.03375 g)), and 1-hexadecylamine (HDA, 0.971 g, 4 mmol) was heated to 120 °C under vacuum for 30 min. The MW vessel was inserted into the MW cavity and heated at 300 W to 240 °C for 15 min. The solution was cooled to 50 °C, and the Eu:Y_2O_3 nanocrystals were precipitated by addition of toluene (~5 mL) followed by MeOH (~5 mL). The product was isolated for centrifugation, washed four times using toluene/MeOH, and dried under vacuum overnight. The isolated sample is tan in color and can be dispersed in toluene.

Measurements. TGA (thermogravimetric analysis) data were recorded on a TA SDT Q600 instrument. FT-IR spectra were measured on a Perkin-Elmer Spectrum GX system in KBr. The FT-IR spectra on samples that had been annealed at 20, 200, 300, 400, and 500 °C were conducted on individual samples that were premixed with KBr (1.33 mg of Eu:Y_2O_3 with 100 mg of KBr) and then thermally annealed prior to pressing the pellet. The thermal annealing of individual samples allows quantitative analysis of the FT-IR spectral intensity changes.

Elemental composition analysis was performed by X-ray fluorescence for Y and Eu. The measurements were carried out on an Oxford Instruments ED_{2000} X-ray fluorescence spectrometer with a Cu Kα source. The concentrations were measured for Eu at 5.8 and 14.9 keV, corresponding to the Lα and Kα lines respectively. All of the measurements were performed by complete dissolution of the solid samples in 90% HNO_3, then the solutions were heated until clear, at which point all excess NO_x had been driven off. The samples were diluted to a volume of 3 mL using 2% HNO_3. In order to generate a calibration curve for the molar concentration of Eu, an appropriate amount of $EuCl_2$ was dissolved in 2% HNO_3 to make a 1000 ppm standard, which was then further diluted to get 800, 600, 400, 200, 100, 50, and 20 ppm solutions. The calibration curve for Y was generated by using a commercially prepared 1000 ppm elemental standard in 2% HNO_3, which was then diluted in the same fashion as above.

Solid-state $^{13}C\{^1H\}$ CP-MAS NMR experiments were performed on a Varian Unity/Inova 11.75 T spectrometer with a Chemagnetics triple-resonance probe. The probe was tuned to 500.3 MHz for ^1H and 125.8 MHz for ^{13}C, and the third channel was not used. Measurements of Y(acac)$_3$ by $^{13}C\{^1H\}$ CP-MAS spectra were acquired in a 4 mm probe at 12 kHz using ^1H decoupling, ramped cross-polarization (CP), an acquisition time of 50 ms, a recycling delay of 2 s, a 90° pulse length of 5 μs, and a 1 ms contact time. Measurements of the Y_2O_3 and Eu:Y_2O_3 nanocrystal by $^{13}C\{^1H\}$ CP-MAS spectra were acquired in a 2.5 mm probe at 15 kHz using ^1H decoupling, ramped cross-polarization (CP), an acquisition time of 20 ms, a recycling delay of 4 s, a 90° pulse length of 5 μs, and a 1 ms contact time.

Structural characterization was performed using powder X-ray diffraction (pXRD) recorded on a Rigaku DMAX 300 Ultima III Powder X-ray diffractometer (using Cu Kα λ = 1.5418 Å radiation). Size, size dispersity, morphology, and structure were analyzed by TEM using a JEOL-2010 microscope operated at 200 kV. The samples were dispersed on holey carbon grids (400 mesh) from a toluene solution. Size and size dispersity were extracted by analysis of 17 TEM images representing 443 nanocrystals (Figure S1 in the Supporting Information shows a selection of the micrographs).

Fluorescence spectra were recorded at room temperature using a Spex Fluorolog II equipped with 0.22 m double monochromators (Spex 1680) and a 450 W Hg lamp. Selective excitation spectra for the Eu(III) $^7F_0 \rightarrow {}^5D_0$ was performed at room temperature by excitation using the output of a dye laser containing Rhodamine 590 and Rhodamine 610 pumped by a Nd−YAG laser. The photoluminescence was collected at 90°, analyzed using a 0.25 m monochromator (slit 1.5 mm, 1180 grooves/mm) coupled to a Hamamatsu R928 photomultiplier tube, and recorded through an oscilloscope interfaced with a computer.

Absolute solid-state quantum yields were measured on the powdered samples following literature procedures[66] using a Spex Fluorolog 2 equipped with 250 mm double monochromators in which is mounted a 4.2 cm diameter integrating sphere (Labsphere). The excitation source consists of a NIST-calibrated Hg lamp. The number of photons emitted from the phosphor is integrated from 380 to 780 nm to calculate the emission quantum yield. Measurement of the diffuse scattered light at 90° from the excitation pathway was carried out in accordance with the technical bulletin from Jobin-Horiba. Spectra of the scattered light were recorded with and without the sample in the sphere. Integration of the area beneath the excitation light is proportional to the total number of incident photons for the first spectrum and to the number of nonabsorbed photons for the second spectrum. The difference between these two is the number of absorbed photons. Integrating the area under the fluorescence peak from the second spectrum gives the emitted photons. By definition, the fluorescence quantum yield is the number of emitted photons divided by the number of absorbed photons. Use of a NIST-calibrated Hg lamp coupled to the integrating sphere allows accurate measurement of the light flux (photons), integrating sphere response function, and the phosphor quantum yield following lamp excitation. The measurement is validated by comparison to the solid-state quantum yield standard, sodium salicylate.

Fabrication of a prototype solid-state lighting device was prepared by removal of the LED lens (0.4 mm from the wire bond or reflective cavity) from a commercial 370 nm excitation LED (TH-UV365GG, 365/370 m) and coating the exposed LED surface with the phosphor dissolved in cyanoacrylate (Super Glue). The phosphor is deposited as a thin film onto the LED surface and prepared by mixing 0.1 g of Eu:Y_2O_3 with 0.3−0.4 g of Super Glue. The device was operated at 3.0 V. The values for CIE coordinates (Commission Internationale de l'éclairage), the color-coordinated temperature (CCT), the S/P (scotopic-to-photopic) ratio, and the luminous efficiency were obtained as described in the literature.[5,7,8,67]

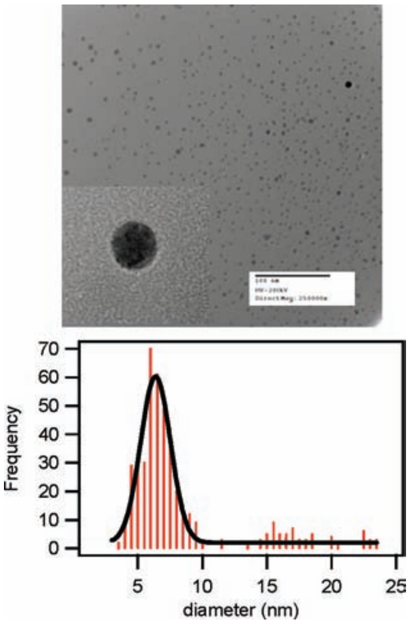

Figure 1. (top) TEM micrograph of 6.4 ± 1.5 nm Eu (2%):Y_2O_3 imaged at 200 keV (250 000×) on a 400 mesh amorphous carbon grid (scale bar 100 nm). Inset: image of a single Eu:Y_2O_3 nanocrystal at 1 500 000× magnification. (bottom) Size distribution of Eu(2%):Y_2O_3 measured over 433 particles in the TEM.

RESULTS

Characterization of Eu:Y_2O_3. The synthesis of Eu(III)-doped Y_2O_3 nanocrystals prepared by microwave (MW)-assisted thermal decomposition of Eu(acac)$_3$ and Y(acac)$_3$ at 240 °C (300 W) in hexadecylamine (HDA), a non-MW-absorbing, nonhydrolytic solvent, produces spherical 6.4 ± 1.5 nm Eu:Y_2O_3 nanocrystals with a tail in the distribution toward larger particles, as shown for the 2% Eu:Y_2O_3 nanocrystal (Figure 1; larger images and several micrographs are available in Figure S1 in the Supporting Information). The distribution was measured over 433 nanoparticles. The well-dispersed spherical morphology nanocrystal distribution is consistent with Ostwald ripening growth behavior under the experimental conditions. The reactions are complete within 15 min. The nanocrystals are doped at 0% (Y_2O_3), 2.3% (2% Eu:Y_2O_3), 8.6% (9% Eu:Y_2O_3), 11.4% (11% Eu:Y_2O_3), and 17.6% (18% Eu:Y_2O_3) Eu(III) by control of the initial reaction stoichiometry, as verified by X-ray fluorescence analysis of the samples.

Structural characterization of the isolated Eu:Y_2O_3 nanocrystal is achieved by measurement of the pXRD and TEM electron diffraction (Figure 2). The pXRD pattern in Figure 2 for the Eu:Y_2O_3 nanocrystal can be indexed to a cubic structure (JCPDS card 43-1036) with well-defined (222), (123), (400), (440), (145), (622), and (662) diffraction peaks. Comparison of the observed pXRD intensities to the bulk standard card reveals the (123) and (145) diffraction intensities are enhanced in the nanocrystal relative to a bulk powder. Confirmation of the pXRD cubic phase assignment is provided by the TEM electron diffraction pattern in Figure 2 (inset), where the (222) and (440) diffractions are clearly observed. The enhancement of the (123) and (145) diffractions in the pXRD is believed to reflect ligand control over the nanocrystal faceting during growth due to the strong coordination of acac to an oxygen-rich facet of the core

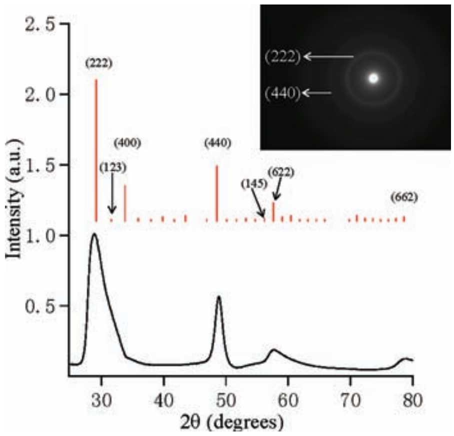

Figure 2. pXRD spectra of Eu(2%):Y_2O_3 in comparison to the standard card for the cubic phase of Y_2O_3 (JCPDS 43-1036). Inset: TEM - electron diffraction pattern with plane assignments for the Eu:Y_2O_3 nanocrystal.

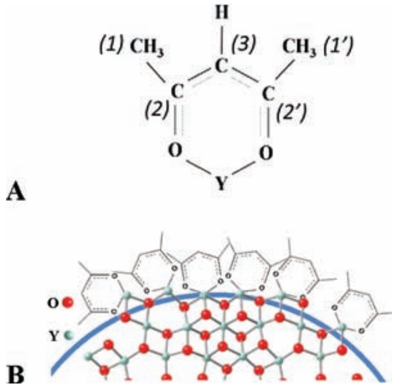

Figure 3. (A) Type A bridging bidentate coordination of acac to yttrium. The numbers in parentheses label the carbons as a reference. (B) Proposed octahedral coordination of acac to the (222) lattice plane of Eu:Y_2O_3 in the cubic crystal structure (JCPDS card 43-1036).

nanocrystal or coordination of acac via the oxygen to a Y-rich facet of the core nanocrystal (Figure 3). Selective face adsorption of ligands is known to influence nanocrystal growth in CdSe quantum dots.[68] Observation of the normally weak (123) and (145) pXRD features has been observed previously in the pXRD of Y_2O_3 and Eu_2O_3 nanocrystals passivated with oleic acid.[18,69]

Surface Passivation Layer of Eu:Y_2O_3. The nanophosphor surface passivation can be analyzed by analysis of the FT-IR (Figure 4A) and $^{13}C\{^1H\}$ CP-MAS NMR (Figure 4B). In the FT-IR spectra of acac−Eu (2%):Y_2O_3, the IR vibration at 565 cm^{-1} is assignable to the Y−O vibration for Y_2O_3, which occurs at a frequency identical with the IR-active optical phonon in cubic Y_2O_3, confirming formation of the cubic lattice.[70] The surface passivant exhibits IR vibrations between 700 and 3000 cm^{-1}. Although the acac and HDA absorptions strongly overlap, evidence for both HDA and acac binding is provided by comparison to the FT-IR spectra of Y(acac)$_3$, Eu(acac)$_3$, Eu:Y_2O_3, and HDA (Figure SF2, Supporting Information).

In the FT-IR spectra of the Eu(2%):Y_2O_3 nanocrystals in Figure 4A, the vibration at 659 cm^{-1} can be assigned as an acac skeletal deformation mode, the 1025 cm^{-1} mode is assigned to a $-CH_3$ rocking mode (P_x) on the acac, and symmetric and antisymmetric acac vibrations for the ν(C=C,C=O) can be assigned at 1403 and 1525 cm^{-1}, respectively. The $\Delta\nu$(C=C, C=O) value of 122 cm^{-1} is typical for a nonbridging bidentate type A coordination of the acac to the metal center, as shown in Figure 3A.[71] The presence of HDA as a passivant is confirmed by the observation of the $-CH_2$ symmetric and asymmetric stretches at $\nu_s(-CH_2)$ 2854 cm^{-1}, and $\nu_{as}(-CH_2)$ 2925 cm^{-1}, which arise at identical frequencies for HDA surface passivation in CdSe QDs.[72] The HDA $-CH_2$ deformation mode at 1471 cm^{-1}, which is much weaker than the stretch, overlaps the acac IR absorption and cannot be definitively assigned. From the intensity of the $\nu_s(-CH_2)$ and $\nu_{as}(-CH_2)$ stretch to the acac ν(C=C,C=O), the HDA is a minor passivant of the isolated nanocrystal. The FT-IR data for HDA, Y(acac)$_3$, Eu(acac)$_3$, and acac-Eu:Y_2O_3 are collated and assigned in Table ST1 in the Supporting Information.

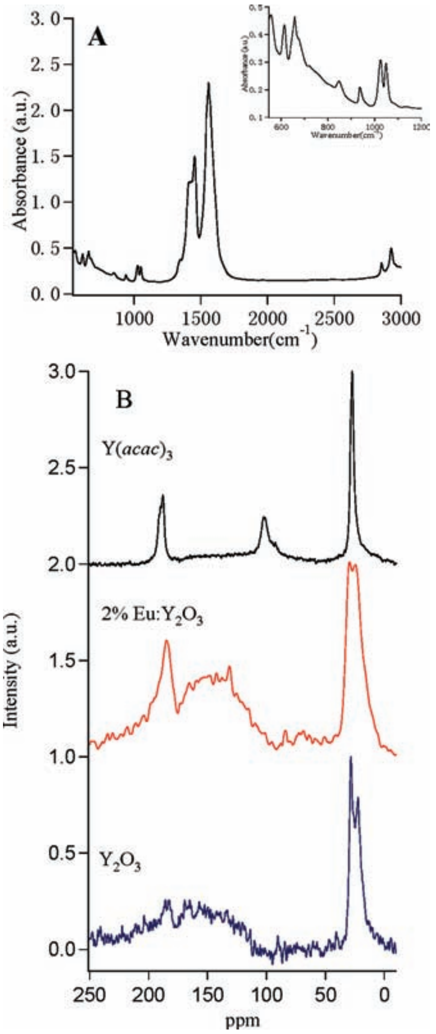

Figure 4. Surface passivation layer characterization data for 6.4 ± 1.5 nm acac-passivated Eu:Y_2O_3 nanocrystals: (A) FT-IR spectra of Eu:Y_2O_3 illustrating mid-frequency IR data and (in the inset) low-frequency IR data; (B) $^{13}C\{^1H\}$ CP-MAS spectra for Y(acac)$_3$ (black), acac−Eu:Y_2O_3 (red), and acac−Y_2O_3 (blue).

The experimental results indicating acac and HDA binding to the nanocrystal surface are further supported by solid-state $^{13}C\{^1H\}$ CP-MAS NMR measurements on the acac-Y_2O_3 and acac-Eu(2%):Y_2O_3 nanocrystals by comparison to Y(acac)$_3$ in

Figure 4. No measurements were carried out on Eu(acac)$_3$ or the higher doped samples of acac-Eu:Y_2O_3, due to the large paramagnetic broadening and lanthanide shift observed for Eu(III) coordination complexes that result in loss of the NMR signal.[73]

The ^{13}C NMR spectrum for Y(acac)$_3$ exhibits identifiable acac features for type A coordination[74] at 24.8 ppm (^{13}C(1,1′) for the $-CH_3$ on acac), 191.3 ppm (^{13}C(2,2′) for the C═O in acac), and 100.5 ppm (^{13}C(3) for the >C in acac). The numbering of the carbons of acac refers to Figure 3. The solid-state ^{13}C NMR for Y_2O_3 shows ^{13}C NMR features consistent with acac and HDA, as evidenced by a set of sharp features at 19, 23, and 29 ppm and a broad feature between 100 and 160 ppm. The feature at 23 ppm is assigned as the ^{13}C(1,1′) for the $-CH_3$ on acac, the 29 ppm feature is assigned to the $-CH_2$ units on HDA,[75] and the feature at 19 ppm is assigned as the $-CH_3$ group in HDA. The broad feature arises from a superposition of the ^{13}C on acac at positions 2,2′ and 3 for the ligand. The line broadening of the ^{13}C(2,2′ and 3) reflects the restricted rotational freedom for the bound acac centers and possible contributions from a distribution of binding motifs. The observation of the sharp feature for the ^{13}C(1,1′) position is due to the free rotation of the $-CH_3$ group in the acac ligand. Similar observations of extreme line broadening following ligand passivation of a nanocrystal have been reported.[75]

The intensity of the features cannot be used to assign the composition of the passivation layer, since the solid-state measurement is a ^{13}C{^{1}H} CP-MAS NMR experiment where the intensity of the CP-MAS experiment will be influenced by a combination of ^{13}C population, cross-polarization time, rise time, and proton pool distance and availability.[76] Although predicting the concentration of the acac to HDA is not achievable, it is clear the HDA concentration is substantially lower than that of the acac, since the HDA has more ^{13}C and a larger proton pool; however, the acac to HDA signal is smaller. The NMR results, therefore, are in agreement with the IR data, suggesting HDA and acac passivate the nanocrystal surface, with acac being the dominate passivant.

The ^{13}C NMR for Eu(2%):Y_2O_3 exhibits features at 24.4, 29.6, 140 (broad), and 185 ppm. The features at 24.4 and 29.6 ppm can be assigned to the $-^{13}CH_2$ on HDA and the $-^{13}CH_3$ (1,1′) on acac, respectively. The $-^{13}CH_3$ HDA feature at 19 ppm is absent, most likely due to broadening of the NMR features obscuring the peak. The broadening of the NMR feature is due to the restricted rotation of the acac and HDA passivant shell on the nanocrystal surface.[75] The most notable spectral change is the change of the broad, featureless peak in the 100−160 ppm region observed in Y_2O_3. In the Eu:Y_2O_3 NMR, a sharp feature at 185 ppm is observed, as well as a sharpening of the broad feature (center position at 140 ppm). The changes in the ^{13}C NMR spectra reflect contributions from a paramagnetic shift and dipolar broadening due to the presence of the Eu(III) ion.[73] Eu(III) diketonate agents are routinely employed as lanthanide shift reagents, and the peak shift is distance and concentration dependent.[73] In the case of the Eu:Y_2O_3 sample, the shift will be complicated by the fact that the Eu−acac distances represent an ensemble across the 16 nm nanocrystal and possible variable bonding motifs. In the solid-state NMR the 185 ppm peak arises from ^{13}C(2,2′,>C═O) for acac. In Y(acac)$_3$ the ^{13}C(2,2′,>C═O) peak is observed at 191 ppm. The small shift for the C═O is expected, due to the dipolar effect of the lanthanide shift reagent and long contact distances at the low doping concentration. The narrowing of the feature reflects a change in the relaxation rate due to changes in the CP-MAS matching conditions. No attempt was made to further optimize the CP conditions, due to the corroboration of the IR and NMR results. The broad feature from 100 to 160 ppm (center at 140 ppm) is therefore assigned to the ^{13}C(3,3′,>C) group on acac, which is broadened due to restricted rotation, and ^{13}C(2,2′,>C═O) on acac not in the vicinity of the Eu(III) ion.

Although the NMR data are broadened by the binding of acac and HDA to the nanophosphor surface, the data support a model in which HDA and acac are bound to the nanocrystal surface in a type A confirmation. The number of acac groups per Y (or Eu) ions at the nanocrystal facet will be equal to 1 or more in order to accommodate the typical >6 coordination number observed for passivation of Ln(III) ions.[58] Further insight into the structure at the surface cannot be determined from the structural, vibrational, and NMR results. Experimental observation of acac acting as a passivating ligand has been previously reported in PZT (lead zirconate titanate) nanocrystals prepared from metal acac precursors in nonhydrolytic solvents.[77]

Optical Properties of Eu:Y_2O_3. In Eu^{3+} doped into bulk yttria no visible absorption features below 300 nm are observed; however, visible emission is observed from the Eu(III) J-O transitions that are efficiently populated following excitation into the yttria excitonic levels ($O_{2p} \rightarrow Y$), the Eu(III) CT ($O_{2p} \rightarrow Eu$), or the higher lying f−f levels of Eu(III). In Eu(III), the optically observed Judd-Ofelt (J-O) transitions can be assigned as electric dipole and magnetic dipole allowed Eu(III) $^5D_0 \rightarrow {}^7F_J$ ($J = 1-4$) transitions. The observed electric dipole transitions are the $^5D_0 \rightarrow {}^7F_J$ ($J = 2-4$) for Eu(III), where $J = 3$ is weak and $J = 2, 4$ are strong. The $^5D_0 \rightarrow {}^7F_1$ line is a magnetic dipole transition allowed by selection rules of $J = 0, \pm 1$. Doping Eu(III) into bulk Y_2O_3 results in two possible sites of occupation, namely a site with inversion symmetry and a site with no inversion symmetry. The $^5D_0 \rightarrow {}^7F_2$ electronically allowed transition gains intensity relative to the $^5D_0 \rightarrow {}^7F_1$ transition when Eu(III) ions occupy a site without inversion symmetry.[48,49]

The population of the Eu(III) J-O levels following excitation into the higher lying electronic states occurs by intramolecular energy transfer via nonradiative paths.[57] The efficiency of the downconversion process is concentration dependent and is known to be impacted by Eu−Eu deactivation pathways at high Eu concentrations.[54] The observed intensities of the J-O transitions in Eu:Y_2O_3 nanocrystals will be influenced by the crystal lattice, the passivating ligand, the RE ion concentration, and the symmetry and site of doping of the Eu(III) guest ion.

The acac−Eu:Y_2O_3 nanocrystals in this study exhibit low-energy absorptions due to the presence of the $S_o \rightarrow S_1$ $\pi \rightarrow \pi^*$ acac and acac to lanthanide LMCT transitions present in these materials. Due to the presence of these ligand-based transitions, the acac−Eu:Y_2O_3 nanocrystals can be pumped at energies lower than 300 nm and through intramolecular energy transfer populate the J-O levels of Eu(III). Representative optical data (absorption, photoluminescence (PL), and photoluminescence excitation (PLE)) for the Eu (2%):Y_2O_3 nanocrystal are shown in Figure 5. Optical data for 0%, 2%, 9%, 11%, and 18% Eu-doped Y_2O_3 are provided in Figures SF3 (photoluminescence) and SF4 (photoluminescence excitation) in the Supporting Information.

Absorption. The solution-phase optical absorption spectrum in CH_3CN for the Eu (2%):Y_2O_3 nanocrystal compared to those of Eu(acac)$_3$ and Y(acac)$_3$ is shown in Figure 5A. The absorption band observed at 270 nm is assignable to the $S_0 \rightarrow S_1$ $\pi \rightarrow \pi^*$ molecular orbital transition for acac by comparison to literature

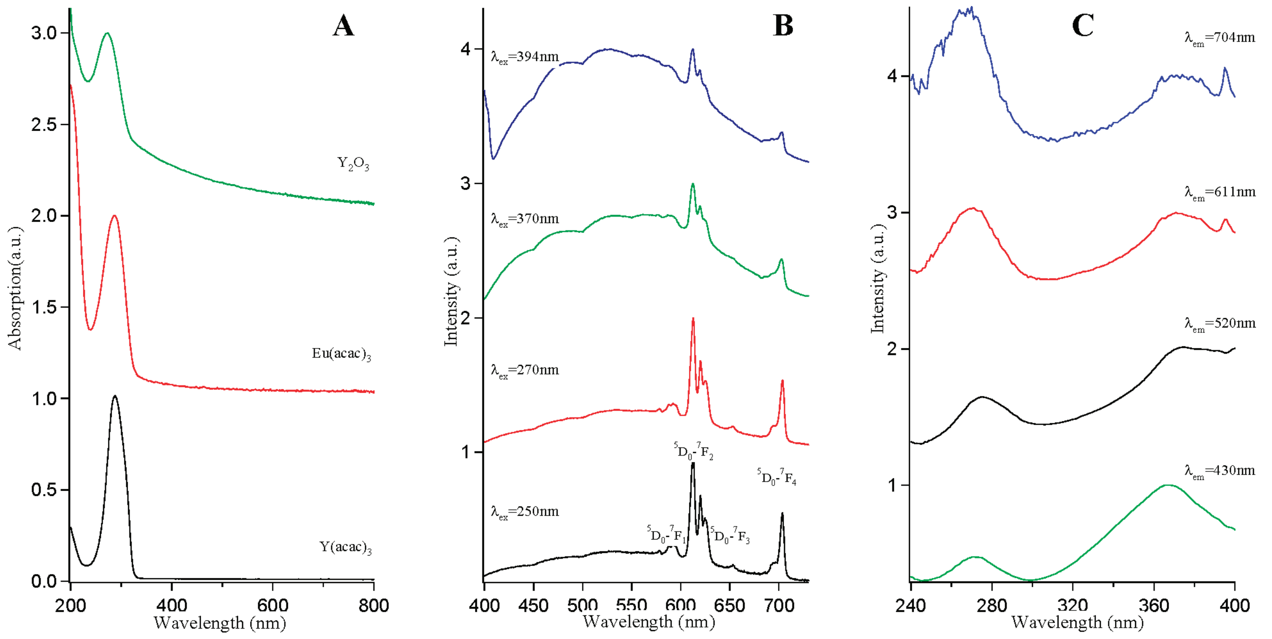

Figure 5. (A) Solution UV−vis absorption spectra in CH_3CN of acac−Eu:Y_2O_3, $Eu(acac)_3$, and Y(acac). (B) Solid-state photoluminescence (PL) spectra (298 K, λ_{ex} 250, 270, 370, and 394 nm) of acac−Eu:Y_2O_3. (C) Solid-state photoluminescence excitation (PLE) spectra (298 K, λ_{em} 430, 520, 611, 704 nm) of acac−Eu:Y_2O_3.

values[48,49] and the RE acac coordination compounds in Figure 5A. It is known that the energy of the $S_0 \rightarrow S_1$ $\pi \rightarrow \pi^*$ acac transition is not strongly influenced by the lanthanide ion.[48,49] The lower energy tail arises from scattering due to the low solubility of the nanocrystals. The observation of the $S_0 \rightarrow S_1$ $\pi \rightarrow \pi^*$ acac transition is consistent with the presence of acac bound to the nanocrystal surface. The expected higher energy ∼210 nm Y_2O_3 band gap absorption ($O_{2p} \rightarrow Y_{5s}$, $E_g(Y_2O_3)$ = 6.0 eV), charge transfer transition $O_{2p} \rightarrow Eu_{4f}$ at 250 nm, and Eu(III) f−f allowed transitions occurring at 394 nm ($^7F_0 \rightarrow {}^5L_6$) and 465 nm ($^7F_0 \rightarrow {}^5D_2$) are not resolved in the solution absorption spectrum.[17,78]

Photoluminescence. Photoluminescence (PL) spectra for the Eu(2%):Y_2O_3 sample are shown in Figure 5B excited into the energy of the $O_{2p} \rightarrow Eu_{4f}$ CT transition at 250 nm,[17] the acac $S_0 \rightarrow S_1$ $\pi \rightarrow \pi^*$ transition at 270 nm,[47] the $O_{(acac)} \rightarrow$ Ln(III) LMCT transition at 370 nm,[47] and directly into the Eu(III) $^7F_0 \rightarrow {}^5L_6$ transition at 394 nm. The concentration-dependent PL behavior is shown in Figures S3A (270 nm) and S3B in the Supporting Information (370 nm).

For all excitations, the observed PL spectra in Figure 5B consist of a set of sharp features characteristic of Eu(III) f−f allowed Judd-Ofelt (J-O) $^5D_0 \rightarrow {}^7F_J$ (J = 1−4) transitions between 580 and 710 nm overlapped by a broad PL feature centered at 520 nm (range 400−700 nm). The intensities of the $^5D_0 \rightarrow {}^7F_J$ transitions increase relative to the Y_2O_3 defect as the Eu(III) doping concentration increases (Figure SF3 in the Supporting Information). The broad feature in the PL spectra centered at 520 nm is assigned to Y_2O_3 oxygen defect PL on the basis of cathodoluminescence measurements carried out in bulk Y_2O_3.[79−81] The features in the broad band can be assigned as arising from PL from oxygen vacancies ($V_O \approx$ 430 nm),[79,80] and recombination centers associated with nearest-neighbor Y(III)−O^{2-} donor−acceptor pairs ($D{-}A_{Y-O(1)}$ ∼653 nm)[79−81] as well as non-nearest-neighbor donor−acceptor pairs for Y(III) and O^{2-} ($D{-}A_{Y-O(2)}$ at ∼480, 520, and 590 nm).[79,80] The sharp features are assigned to the J-O $^5D_0 \rightarrow {}^7F_J$ (J = 1−4) Eu(III) transitions and are labeled in Figure 5B. In the PL data the $^5D_0 \rightarrow {}^7F_2$ line is the strongest, indicating the emissive Eu(II) center occupies a site without inversion symmetry. The Eu(III) electric dipole broadens relative to a bulk sample, as shown by the line width of the $^5D_0 \rightarrow {}^7F_2$ transition in the nanocrystal of 0.018 eV vs that in bulk of 0.009 eV (Figure SF5 in the Supporting Information).

The wavelength dependence of the PL spectra for the Eu:Y_2O_3 in Figure 5B is telling with respect to the intramolecular energy transfer cascade from the initial absorption of incident light by the CT ($O_{2p} \rightarrow Eu_{4f}$) and $S_0 \rightarrow S_1$ ($\pi \rightarrow \pi^*$, acac) in the UV or the LMCT transition from acac to the Ln(III) ions to the emissive Eu(III) dopant sites. Excitation into the $O_{2p} \rightarrow Eu_{4f}$ CT transition at 250 nm or the acac $\pi \rightarrow \pi^*$ transition at 270 nm leads to the efficient population of the J-O $^5D_0 \rightarrow {}^7F_J$ transitions for Eu(III) with minimal population of the Y_2O_3 defect levels. The efficient relaxation from the initially populated S_1 state or CT state to the Eu(II) f−f levels indicates that the intersystem crossing to the acac T_1 and subsequent nonradiative relaxation to the Eu(III) J-O levels arise from an efficient phonon-assisted process.

The concentration-dependent absolute solid-state quantum efficiencies (ϕ_{em}) measured in an integrating sphere for the acac−Eu:Y_2O_3 pumped at 270 nm are 1% for Eu (0%), 7% for Eu (2%), 12% for Eu (9%), 9% for Eu (11%), and 8% for Eu (18%). The concentration-dependent quantum efficiency is typical of Eu(III) self-quenching arising at higher concentrations and the depopulation of the C_2 Eu(III) site by the S_6 (C_{3i}) site, which has been shown to reduce the quantum efficiency in bulk materials at higher Eu concentration.[54]

Excitation into the $O_{acac} \rightarrow$ Y(III) LMCT transition at 370 nm or directly into the Eu(III) $^7F_0 \rightarrow {}^5L_6$ transition at 394 nm results in an increased contribution from the Y_2O_3 oxygen defect energy

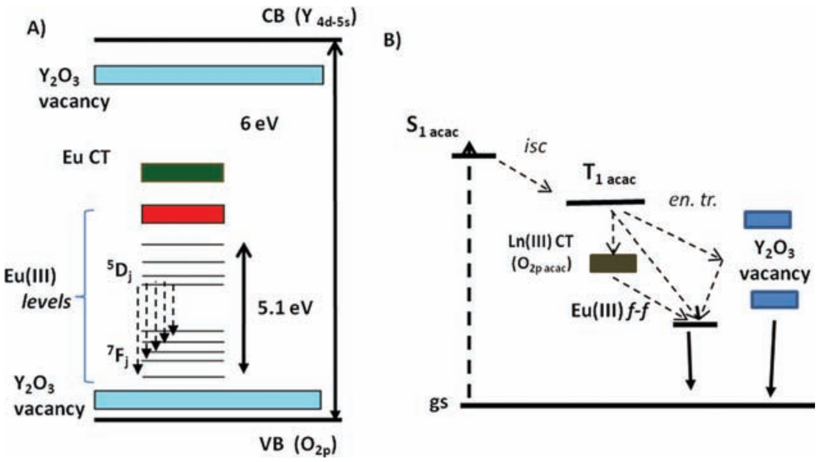

Figure 6. (A) Schematic energy level diagram and (B) relaxation pathways for efficient downconversion to the Eu(III) J-O transitions and Y_2O_3 defect levels in the acac−Eu:Y_2O_3 nanocrystals.

levels and the production of a white light phosphor spectrum. The quantum efficiencies for acac−Eu:Y_2O_3 pumped at 370 nm of 11% Eu (0%), 14% Eu (2%), 19% Eu (9%), 13% Eu (11%), and 10% Eu (18%) show a smaller concentration dependence, indicating population of the Y defect levels does not efficiently populate the Eu(III) f−f J-O levels due to the inefficient energetic or phonon coupling of the defect levels in Y_2O_3 to the J-O levels in Eu(III) or due to formation of a trapped excitonic state at the defect centers in the lattice. The increased intensity of the defects for optical pumping at 394 nm is more surprising and likely reflects the competition between direct population of the vacancy levels and the low optical cross section Eu(III) f−f levels. Further insight into the energy funneling mechanism to the Eu(III) center can be gained by inspection of the wavelength-dependent photoluminescence excitation spectra.

Photoluminescence Excitation. Photoluminescence excitation (PLE) spectra monitored at selected wavelengths can provide spectral evidence of the excited state partitioning between the Y_2O_3 defect and Eu(III) J-O levels following initial excitation. The wavelength-dependent PLE data for the 2% Eu:Y_2O_3 nanocrystal is shown in Figure 5C monitored at the energy of the $^5D_0 \rightarrow {}^7F_2$ Eu(III) transition at 611 nm, the $^5D_0 \rightarrow {}^7F_4$ Eu(III) transition at 704 nm, the V_0 defect at 430 nm, and the $DA_{Y-O(1)}$ defect at 520 nm. The PLE spectra exhibits two broad PLE features centered at 270 and 370 nm regardless of the monitoring energy. The PLE feature observed at 270 nm can be assigned to the acac $S_0 \rightarrow S_1$ $\pi \rightarrow \pi^*$ transition, as observed in the solution absorption spectra (Figure 5A). The PLE feature at 370 nm can be assigned to the acac $O_{acac} \rightarrow$ Y(III) LMCT transition by comparison to the absorption features reported for $Ln(acac)_3$ coordination complexes.[47] Monitoring at 611 and 704 nm, which correspond to the Eu(III) J-O transitions, results in the additional observation of the Eu(III) $^7F_0 \rightarrow {}^5L_6$ level at 394 nm.[82] The recorded PLE spectra in Figure 5C are notable for several reasons in comparison to the PLE reported for either bulk[83] or nanocrystalline Eu:Y_2O_3:[17] (i) the appearance of PLE features at 270 and 370 nm, (ii) the PLE feature at 270 nm increasing in intensity relative to the feature at 370 nm as the monitoring wavelength for the PLE spectra is shifted to the red, and (iii) the lack of a 250 nm transition for the $O_{2p} \rightarrow Eu_{4f}$ CT transition. The strong PLE features observed at energies consistent with the presence of acac passivation indicate that the Ln−acac passivant can efficiently absorb and transfer energy to the Eu(III) centers. The lack of a 250 nm transition in the PLE can be attributed to the lower cross section for absorption of the $O_{2p} \rightarrow Eu(III)_{4f}$ CT transition in comparison to the optical cross section for the acac electronic transitions.

The appearance of the Eu(III) $^7F_0 \rightarrow {}^5L_6$ is not surprising when the J-O level is probed, but the appearance of the LMCT and $S_0 \rightarrow S_1$ $\pi \rightarrow \pi^*$ transition associated with acac passivation of the nanocrystal surface is somewhat surprising and suggests direct excitation into the $\pi-\pi^*$ acac transition results in efficient energy transfer to the Eu(III) centers in the host lattice via a phonon-assisted process or Eu−Eu pair activation leading to excitation of one Eu(III) emissive center to a high-lying level and depopulation of the other Eu(III) pair ion.[54] Although the results suggest that energy transfer from the high-lying acac transitions is efficient in these materials, the initial excited-state population partitions into a phonon-assisted relaxation into the Eu(III) J-O levels and separately can be trapped by the internal lattice defects. The defect levels are believed to represent local defect radiative trap centers and due to site trapping exhibit poor energy transfer to the Eu J-O levels. Cross population from the defects to the J-O levels appears to be inefficient, reflecting the large separation distance between the defect and Eu(III) center at low doping concentrations. Excitation into the lower energy $O_{acac} \rightarrow$ Ln(III) leads primarily to the population of the Y_2O_3 defect energy levels, implying that the energy gap between the LMCT transition and the Eu(III) J-O levels does not allow efficient depopulation, since the process is anticipated to be a random walk process following a dipole−dipole exchange mechanism. In $Eu(acac)_3$ poor population of the Eu J-O levels was similarly observed to arise from a competition with the LMCT levels, leading to vibrational relaxation via nonradiative pathways.[48,49,54] On the basis of the optical results, a *simplified* schematic for the energy relaxation pathway to the Eu(III) center is shown in Figure 6. The relative intensity of the optical features feature in Figure 5 can be understood in terms of the energy relaxation pathway in Figure 6, due to differences in efficiency for energy transfer from the initially populated acac electronic levels to the lower energy electronic levels in the Y_2O_3 defects and Eu(III) dopant centers.

Evidence of the Presence of Surface and Core Eu(III) Sites in the Eu:Y_2O_3 Nanocrystal. In nanocrystal samples of Eu:Y_2O_3, the intensity and energy of the parity-forbidden Eu(III) $^7F_0 \rightarrow {}^5D_0$

transition is often used as a sensitive probe of the Eu(III) site.[84] In a bulk sample of Y_2O_3, the Eu(III) center can occupy either a C_2 or a S_6 symmetry site. Eu(III) ions occupying the C_2 site leads to the parity-forbidden $^7F_0 \rightarrow {}^5D_0$ transition becoming partially allowed and in nanocrystals is observed to split reflecting contributions from Eu(III) centers occupying a surface and core site in the nanocrystal.[84] In Figure 7, the PLE spectrum for the parity-forbidden $^7F_0 \rightarrow {}^5D_0$ transition monitored at 611 nm ($^5D_0 \rightarrow {}^7F_2$ Eu(III) transition) is shown for the Eu:Y_2O_3 nanocrystal compared to that of a bulk sample. The bulk sample is prepared by sintering the nanocrystal sample at 1000 °C for 2 h. The PLE spectrum for the bulk Eu:Y_2O_3 sample exhibits a single Gaussian transition centered at 580.4 nm, while the nanocrystal exhibits a Gaussian transition at 580.8 nm and a weak transition at 578.9 nm. The similarity in energy of the $^7F_0 \rightarrow {}^5D_0$ parity-forbidden transition for the bulk and nanocrystal samples is consistent with the assignment of the Eu(III) ion occupying a Y(III) C_2 symmetry site as a substitutional element in the Y_2O_3 cubic host lattice. The $^7F_0 \rightarrow {}^5D_0$ transition at 580.8 nm in the nanocrystal sample is assigned to Eu(III) ions occupying a core substitutional site, while the $^7F_0 \rightarrow {}^5D_0$ transition for Eu(III) at 578.8 nm arises from Eu(III) centers near or at the surface of the nanocrystals, as previously reported.[84]

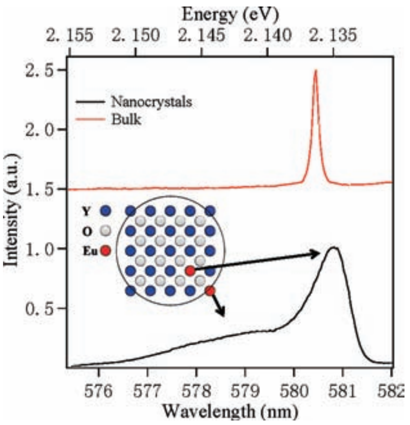

Figure 7. High-resolution PLE spectra for Eu (2%):Y_2O_3 and bulk Eu:Y_2O_3 sample monitored at λ_{em} 611 nm in order to probe the $^7F_0 \rightarrow {}^5D_0$ J-O transition for the Eu(III) C_2 symmetry occupation in the Y_2O_3 host lattice.

Structural Evolution of Nanocrystals Following Thermal Treatment. In Figure 8A, thermogravimetric analysis (TGA) data are shown for the Eu:Y_2O_3 nanocrystal. The changes in the nanocrystal properties following thermal treatment and transformation into a bulk material can provide insight into the stability of the acac passivant layer in the Eu:Y_2O_3 nanocrystal. In the TGA data, a set of sharp transitions is observed at 160, 276, and 379 °C associated with mass losses of ~3, ~6, and ~24%, respectively. Above 379 °C, a continued mass loss of 40% is observed. The mass loss at 160 °C is assigned to solvent loss arising from water or toluene. The transition at 276 °C is assigned to the loss of HDA, as evidenced by the loss of the $-CH_2$ and $-CH_3$ vibrational modes at ~3000 cm^{-1} in the FT-IR spectra (Figure 8B). The transition at 376 °C is assigned to the onset of thermal decomposition of the acac passivating layer on the Eu:Y_2O_3 nanocrystal surface, as confirmed by partial loss of the acac FT-IR transitions at 659, 678 1453, and 1560 cm^{-1} (Figure 8B). Decomposition of acac with subsequent formation of metal oxides and loss of acetone and acetic acid has been observed in a similar temperature range in acac coordination complexes.[85] The mechanism for metal oxide formation in amine solvents has been reported.[86]

No structural transition or particle growth is observed in the pXRD following the loss of the HDA passivant at 276 °C (Figure 8C). A transformation in the pXRD is observed at the 376 °C transition following acac decomposition. The pXRD narrows, and the complete loss of the (123) and (145) diffraction peaks from the pXRD pattern is observed. The change in the pXRD pattern is consistent with nanocrystal growth by particle to particle fusion as the passivating layer decomposes to form a fresh metal oxide surface. Continued growth of Eu:Y_2O_3 is observed in the pXRD up to 1000 °C.

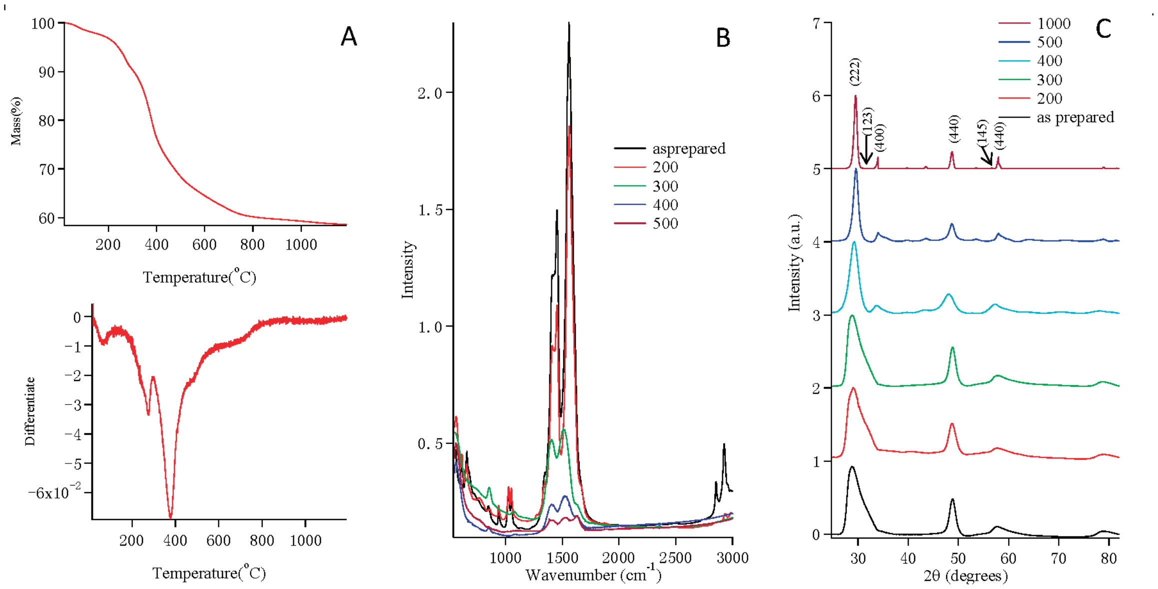

Figure 8. Thermal response for the Eu(2%):Y_2O_3 nanocrystal during thermolysis from 20 to 1000 °C: (A) thermogravimetric analysis (TGA) data and first differential of TGA experimental data; (B) temperature-dependent FT-IR spectra; (C) temperature-dependent pXRD spectra.

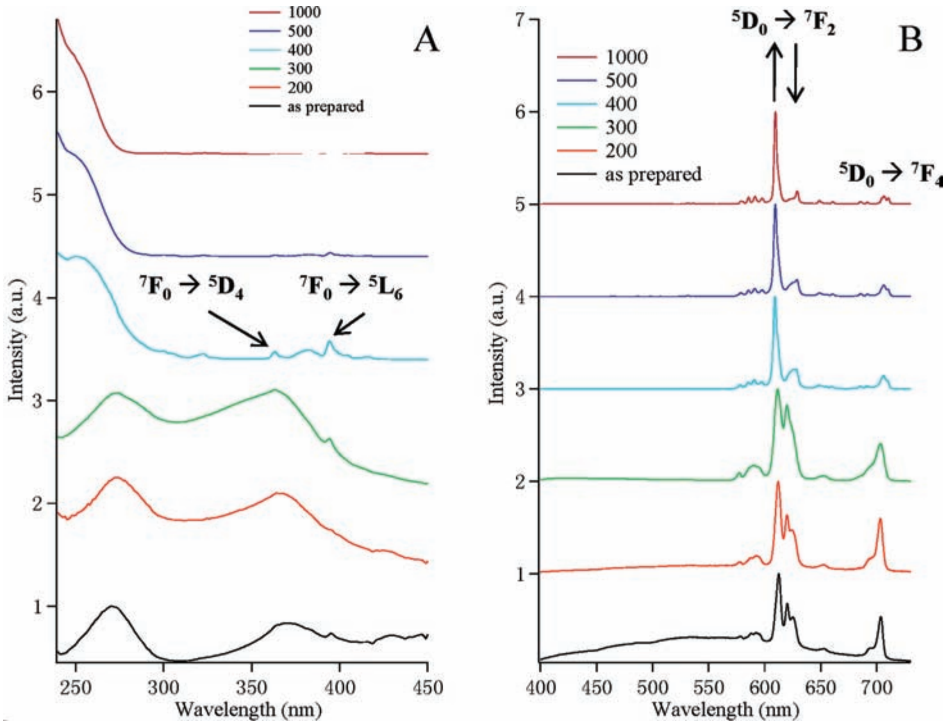

Figure 9. Temperature-dependent changes in the optical properties of Eu (2%):Y_2O_3 nanocrystals during thermolysis from 20 to 1000 °C: (A) solid-state photoluminescence excitation spectra monitored at λ_{em} 611 nm; (B) solid-state photoluminescence spectra, λ_{ex} 270 nm.

Confirming the TGA assignments, no change to the PLE and PL spectra are observed below 400 °C. Above 400 °C, the acac $\pi \rightarrow \pi^*$ (270 nm) transition and acac CT band (370 nm) disappear in the PLE spectra (Figure 9) with a concomitant appearance of the 250 nm lattice CT band typical of bulk Eu:Y_2O_3. Above 400 °C, the reduction in relative intensity of the Eu(III) $^7F_0 \rightarrow {}^5D_4$ and $^7F_0 \rightarrow {}^5L_6$ transitions (labeled with an arrow in Figure 9A) is noted in the PLE spectra, which is believed to be due to the relative strengthening of the lattice CT band ($O_{2p} \rightarrow Eu_{4f}$) as the nanocrystals grow in size. In Figure 9B, the PL spectra (λ_{ex} 270 nm) also exhibits a change above 400 °C, with loss of intensity of the Y_2O_3 defect PL, a narrowing of the J-O transitions, and a redistribution of the intensity in the $^5D_0 \rightarrow {}^7F_2$ Stark-split transitions at 611, 619, and 625 nm. The loss of the defect intensity may reflect the loss of the acac CT transition or changes in Y_2O_3 defect densities in the growing bulk phosphor. The changes in the J-O level as the nanocrystals grow is believed to reflect changes in the core to surface Eu(III) composition with the sintering of the nanocrystal. Consistent with a sintering argument, the PL spectrum of Eu:Y_2O_3 sintered at 1000 °C is directly comparable to that of a bulk phosphor sample.[83] The thermal treatment data indicates that the acac passivation layer is thermally stable below temperatures of 400 °C, which is within the thermal operating range of commercial LED lighting (below 150 °C).

Application of acac-EuY_2O_3 as a Solid-State Phosphor. Eu:Y_2O_3 is a classic downconversion red phosphor used in lighting and display technologies that can be pumped with UV excitation (λ_{em}(Hg line) 254 nm) into the higher lying O_{2p} to $Y_{4d\text{-}5s}$ excitonic level or the Eu(III) CT levels. Nonradiative energy transfer to populate the low-lying Eu(II) J-O levels produce the characteristic red photoluminescence. The lack of electronic transitions with strong optical cross sections for Eu:Y_2O_3 with UV LEDs that exhibit a pump range between 350 and 370 nm limits the use of Eu:Y_2O_3 phosphors in new solid-state lighting devices. The acac passivation layer on the Eu:Y_2O_3 nanocrystal can overcome this limitation, due to the presence of low-lying LMCT states and the acac $\pi \rightarrow \pi^*$ states that exhibit high optical cross sections in the UV spectral region.

The experimental optical data indicate the highest solid-state quantum efficiency for white light generation is for the Eu (9%):Y_2O_3 nanocrystal pumped at 370 nm with a measured ϕ_{em} value of 18.7%. In comparison to the reported quantum efficiency for nanocrystalline samples of Eu:Y_2O_3 prepared by an alkalide reduction method,[87] the highest obtained solid-state quantum yield was ϕ_{em} = 8% pumped at 230 nm, which drops to 2% pumped at 270 nm, and 0% pumped at 370 nm. Although the measured quantum efficiency for the acac–Eu (9%):Y_2O_3 in this study is not at the level of that for the commercial Eu:Y_2O_3 phosphor (90% pumped at 250 nm), the ability to excite the phosphor in the UV (370 nm) and the broad-band white light make the nanophosphor advantageous over the single-color red bulk phosphor when packaged with a UV LED.

In order to generate the quality of the LED phosphor package, a 370 nm LED was coated with the phosphor embedded in cyanoacrylamide and attached to the surface of a declad commercial UV-LED (365/370 nm, 1W), as shown in Figure 10B. Measurement of the red/orange (R/O) ratio, the CIE coordinates (Commission Internationale de l'éclairage), the color coordinated temperature (CCT), the S/P (scotopic-to-photopic) ratio, and the luminous efficiency of the device was carried out.[5−7] Of these, the S/P ratio and luminous efficiency are important for low-light applications. The R/O is phosphor dependent, while the CIE, S/P, and luminosity are device dependent.

The red/orange (R/O) ratio is a critical phosphor quality control value for the Eu(III)-based phosphors and is calculated by comparing the intensity of the $^5D_0 \rightarrow {}^7F_2$ to the $^5D_0 \rightarrow {}^7F_1$

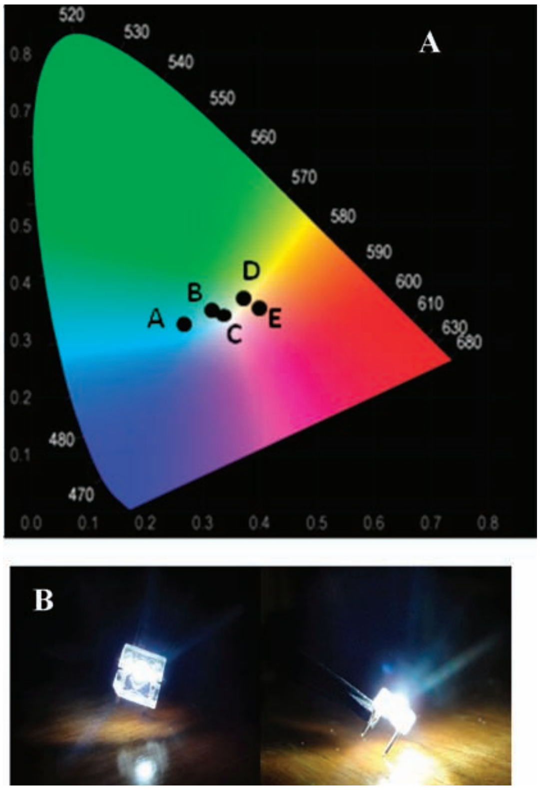

Figure 10. (A) CIE coordinates for Eu:Y_2O_3 doped at (*A*) 0%, (*B*) 2%, (*C*) 9%, (*D*) 11%, and (*E*) 18% plotted on the CIE1930 chromaticity chart. (B) Images of a LED phosphor assembled from deposition of Eu (9%):Y_2O_3 onto a 370 nm LED operating at 3.0 V.

J-O transition. The 9% Eu:Y_2O_3 nanocrystal pumped at 370 or 270 nm has an R/O ratio of 10.1 ± 0.1. In comparison, the R/O ratio for bulk Eu:Y_2O_3 is 6.2, while reported values for non-acac-passivated nanocrystal Eu:Y_2O_3 have reported values ranging from 7 to 9 when pumped at 250 nm.[18]

Figure 10 shows the CIE index points for the Eu:Y_2O_3 compositions prepared in the study, along with a photograph of a white light LED formed using the Eu (9%):Y_2O_3 nanocrystal sample (sample C). The CIE coordinates and CCT values for the acac−Eu:Y_2O_3 at 0% (*A*) is (0.27, 0.32) at 8245 K; 2% (*B*) is (0.32, 0.36) at 6162 K; 9% (*C*) is (0.33, 0.35) at 5418 K; 11% (*D*) is (0.38, 0.38) at 3947 K, and 18% (*E*) is (0.40, 0.36) at 3364 K. As a comparison, incandescent bulbs have a CCT of 2800 K, cool white fluorescent bulbs have a CCT of 6000 K, and daylight is 4500 K.

The S/P ratio is a measure of the perception of white light by the human eye in a dark environment based upon the rod/cone ratio in the human eye. A low value for the S/P ratio is a leading reason for eye fatigue in solid-state lighting.[8] The S/P ratio for the acac−Eu:Y_2O_3 samples are 2.73 Eu (0%), 2.10 Eu (2%), 2.20 Eu (9%), 1.83 Eu (11%), and 1.77 Eu (18%). The S/P ratio for the Eu(III):Y_2O_3 phosphors compares favorably with the S/P ratio for a compact fluorescent light bulb of 2.14.

On the basis of the quantum efficiency, CIE, CCT, and S/P ratio the 9% Eu(III):Y_2O_3 sample produces the highest quality white light and may represent an optimal single-component phosphor for lighting applications using the 370 nm commercial UV-LED.

For the phosphor-LED package to be commercially viable, a luminous efficiency of 100 lm W^{-1} must be achieved. The luminous efficiency (η_L) or luminosity is defined as the amount of light produced for a given device and can be calculated from the luminous flux (ϕ_v) and LED output power (ϕ_e), where $\eta_L = \phi_v/(V_f I_f)$. V_f and I_f are the LED operating voltage and current, respectively, while $\phi_v = \eta_{\text{phosphor}}\phi_e$ (η_{phosphor} is the wavelength conversion efficiency of the phosphor).[7] Measurement of the luminosity of the LED device resulted in a value of 100 lm W^{-1} for the 370 nm LED operating at 3.3 V. The white light LED luminosity drops to ∼80 lm W^{-1} at 3.0 V and below 20 lm W^{-1} at an operating voltage below 3.0 V. A plot of the relative intensity of the white light produced by the device versus applied voltage is plotted in Figure SF6 in the Supporting Information, where the relative intensity is the intensity of the phosphor between 400 and 750 nm collected by an integrating sphere relative to the LED intensity at 370 nm.

■ CONCLUSION

The optical properties of the isolated acac-passivated Eu:Y_2O_3 nanocrystals indicate the samples are ideal phosphors for application as a single-component white light phosphor pumped by a commercial UV-LED. It is clear that the presence of the acac passivation layer on the Eu:Y_2O_3 nanocrystal surface strongly enhances the optical performance of these white light nanophosphors for applications in UV LED pumped solid-state lighting. The phosphor performance outperforms the compact fluorescent light bulb S/P ratio, CIE index, and CCT values. The strong performance reflects the presence of strong acac $\pi \rightarrow \pi^*$ (270 nm) and $O_{acac} \rightarrow$ Y(III) CT (370 nm) transitions arising from the presence of the acac on the nanocrystal surface. The low-energy CT band is not present in bulk Eu:Y_2O_3 phosphors. The observed highly efficient downconversion from the acac CT band to defect levels and the Eu(III) guest ion energy levels suggests that tailoring the design of the metal acac passivation layer could lead to more efficient white light conversion. Such experiments are currently underway.

The paper has developed a novel approach to synthesis and phosphor design. While the use of metal acetylacetonate precursors for the preparation of metal oxide nanocrystals and thin films is not novel,[70,88,89] the observation of the formation of an acac passivation layer that efficiently transfers energy via a molecular antenna from the ligand passivation shell to the Eu(III) J-O levels in Eu:Y_2O_3 and the Y defect levels to produce white light with good color rendition has not been reported. The Eu:Y_2O_3 nanocrystals prepared in a microwave reactor by thermal decomposition of the metal acetylacetonate ($M(acac)_3$) salts in a nonhydrolytic, actively passivating solvent allows rapid preparation (15 min) and isolation of the Eu:Y_2O_3 nanocrystal. The size of the isolated phosphor nanocrystal is not observed to be influenced by reaction concentrations in the MW. It is believed the rapid formation of the nanocrystals reflects the use of MW dielectric heating of the lanthanide coordination compound in a non-MW-absorbing HDA solvent. The rate of reaction in the MW is far faster than in the traditional hydrothermal methods, which require 12 h[17] or hot injection methods, where reaction times of 1 h have been reported.[18] Confirmation of the surface passivation by acac was provided by optical absorption, PLE, $^{13}C\{^1H\}$ CPMAS NMR, and FT-IR analysis.

■ ASSOCIATED CONTENT

Ⓢ Supporting Information. TEM micrographs (Figure SF1), FT-IR spectra (Figure SF2), and Table ST1 reporting IR spectral data and assignments for Eu (2%):Y_2O_3, Y(acac)$_3$, Eu(acac)$_3$, and HDA, wavelength-dependent PL (Figure SF3) and PLE (Figure SF4) spectra for the 0%, 2%, 9%, 11%, and 18% Eu(III)-doped Y_2O_3 nanocrystals, PL spectra of Eu (2%):Y_2O_3 comparing nanocrystal and bulk samples (Figure SF5), and a plot of the relative intensity vs applied voltage for the Eu (9%):Y_2O_3 phosphor coated onto the 370 nm LED (Figure SF6). This material is available free of charge via the Internet at http://pubs.acs.org.

AUTHOR INFORMATION

Corresponding Author

*E-mail: Strouse@chem.fsu.edu.

ACKNOWLEDGMENT

We wish to thank the NSF (Grant No. CHE-0911080) for financial support of the research, Christopher Ridel for assistance in analyzing the Eu(III) concentration, and Dr. Yan Xin for assistance in analyzing the TEM electron diffraction pattern. The TEM measurements were conducted at the NHFML, which is supported through the NSF Cooperative Agreement No. DMR-0654118 and by the State of Florida.

REFERENCES

(1) Schubert, E. F.; Kim, J. K. *Science* **2005**, *308*, 1274–1278.

(2) Justel, T.; Nikol, H.; Ronda, C. *Angew. Chem., Int. Ed.* **1998**, *37*, 3085–3103.

(3) Xu, X. R.; Su, M. Z. *Luminescence and Luminescent Materials*; Chemical Industry Press: Beijing, 2004.

(4) Ronda, C. R. *Luminescent Materials: From Theory to Applications*; Wiley-VCH: New York, 2007.

(5) Chen, G.; Craven, M.; Kim, A.; Munkholm, A.; Watanabe, S.; Camras, M.; Gotz, W.; Steranka, F. *Phys. Status Solidi A* **2008**, *205*, 1086–1092.

(6) Kim, H. S.; Brueckner, E.; Song, J. Z.; Li, Y. H.; Kim, S.; Lu, C. F.; Sulkin, J.; Choquette, K.; Huang, Y. G.; Nuzzo, R. G.; Rogers, J. A. *Proc. Natl. Acad. Sci. U.S.A.* **2011**, *108*, 10072–10077.

(7) Narukawa, Y.; Ichikawa, M.; Sanga, D.; Sano, M.; Mukai, T. *J. Phys. D: Appl. Phys.* **2010**, 43.

(8) Lita, A.; Washington, A. L.; van de Burgt, L.; Strouse, G. F.; Stiegman, A. E. *Adv. Mater.* **2010**, *22*, 3987–3991.

(9) Bowers, M. J.; McBride, J. R.; Rosenthal, S. J. *J. Am. Chem. Soc.* **2005**, *127*, 15378–15379.

(10) Hu, Y. S.; Zhuang, W. D.; Ye, H. Q.; Zhang, S. S.; Fang, Y.; Huang, X. W. *J. Lumin.* **2005**, *111*, 139–145.

(11) Jia, D. D.; Wang, X. J. *Opt. Mater.* **2007**, *30*, 375–379.

(12) He, X. H.; Zhu, Y. *J. Mater. Sci.* **2008**, *43*, 1515–1519.

(13) Shur, M. S.; Zukauskas, A. A. *Proc. IEEE* **2005**, *93*, 1691–1703.

(14) Park, J. K.; Lim, M. A.; Kim, C. H.; Park, H. D.; Park, J. T.; Choi, S. Y. *Appl. Phys. Lett.* **2003**, *82*, 683–685.

(15) Kim, J. S.; Jeon, P. E.; Choi, J. C.; Park, H. L.; Mho, S. I.; Kim, G. C. *Appl. Phys. Lett.* **2004**, *84*, 2931–2933.

(16) Song, H. W.; Chen, B. J.; Peng, H. S.; Zhang, J. S. *Appl. Phys. Lett.* **2002**, *81*, 1776–1778.

(17) Bai, X.; Song, H. W.; Yu, L. X.; Yang, L. M.; Liu, Z. X.; Pan, G. H.; Lu, S. Z.; Ren, X. G.; Lei, Y. Q.; Fan, L. B. *J. Phys. Chem. B* **2005**, *109*, 15236–15242.

(18) Rui, S.; Zhang, Y. W.; Zhou, H. P.; Sun, L. D.; Yan, C. H. *Chem. Mater.* **2007**, *19*, 18–27.

(19) Yada, M.; Mihara, M.; Mouri, S.; Kuroki, M.; Kijima, T. *Adv. Mater.* **2002**, *14*, 309–313.

(20) Hsu, W. P.; Ronnquist, L.; Matijevic, E. *Langmuir* **1988**, *4*, 31–37.

(21) Wakefield, G.; Keron, H. A.; Dobson, P. J.; Hutchison, J. L. *J. Phys. Chem. Solids* **1999**, *60*, 503–508.

(22) Wang, X.; Sun, X. M.; Yu, D. P.; Zou, B. S.; Li, Y. D. *Adv. Mater.* **2003**, *15*, 1442–1445.

(23) Liu, T.; Zhang, Y. H.; Shao, H. Y.; Li, X. G. *Langmuir* **2003**, *19*, 7569–7572.

(24) Cao, Y. C. *J. Am. Chem. Soc.* **2004**, *126*, 7456–7457.

(25) Si, R.; Zhang, Y. W.; You, L. P.; Yan, C. H. *Angew. Chem., Int. Ed.* **2005**, *44*, 3256–3260.

(26) Yu, T.; Joo, J.; Park, Y. I.; Hyeon, T. *J. Am. Chem. Soc.* **2006**, *128*, 1786–1787.

(27) Shin, J. H.; Vandenhoven, G. N.; Polman, A. *Appl. Phys. Lett.* **1995**, *66*, 2379–2381.

(28) Fujii, M.; Yoshida, M.; Kanzawa, Y.; Hayashi, S.; Yamamoto, K. *Appl. Phys. Lett.* **1997**, *71*, 1198–1200.

(29) Wang, X.; Li, Y. D. *Chem. Eur. J.* **2003**, *9*, 5627–5635.

(30) Wang, X. J.; Gao, M. Y. *J. Mater. Chem.* **2006**, *16*, 1360–1365.

(31) Patra, C. R.; Alexandra, G.; Patra, S.; Jacob, D. S.; Gedanken, A.; Landau, A.; Gofer, Y. *New J. Chem.* **2005**, *29*, 733–739.

(32) Mai, H. X.; Zhang, Y. W.; Si, R.; Yan, Z. G.; Sun, L. D.; You, L. P.; Yan, C. H. *J. Am. Chem. Soc.* **2006**, *128*, 6426–6436.

(33) Rao, R. P.; Devine, D. J. *J. Lumin.* **2000**, *87—9*, 1260–1263.

(34) Zhu, W. G.; Jiang, Q.; Lu, Z. Y.; Wei, X. Q.; Xie, M. G.; Zou, D. C.; Tsutsui, T. *Thin Solid Films* **2000**, *363*, 167–169.

(35) Zheng, Y. X.; Liang, Y. J.; Zhang, H. J.; Lin, Q.; Chuan, G.; Wang, S. B. *Mater. Lett.* **2002**, *53*, 52–56.

(36) Kido, J.; Nagai, K.; Okamoto, Y.; Skotheim, T. *Chem. Lett.* **1991**, 1267–1270.

(37) Hu, L. Y.; Song, H. W.; Pan, G. H.; Yan, B.; Qin, R. F.; Dai, Q. L.; Fan, L. B.; Li, S. W.; Bai, X. *J. Lumin.* **2007**, *127*, 371–376.

(38) Park, W. J.; Yoon, S. G.; Yoon, D. H. *J. Electroceram.* **2006**, *17*, 41–44.

(39) Wu, X. Y.; Liang, Y. J.; Chen, R.; Liu, M. Y.; Li, Y. Z. *J. Mater. Chem.* **2011**, *46*, 5581–5586.

(40) Liu, X. M.; Lin, C. K.; Lin, Y. Z. *J. Appl. Phys. Lett.* **2007**, *90*, 081904.

(41) Shang, C. Y.; Shang, X. H.; Qu, Y. Q.; Li, M. C. *Chem. Phys. Lett.* **2011**, *501*, 480–484.

(42) Steffen, M. A.; Lao, K. Q.; Boxer, S. G. *Science* **1994**, *264*, 810–816.

(43) Stowell, M. H. B.; McPhillips, T. M.; Rees, D. C.; Soltis, S. M.; Abresch, E.; Feher, G. *Science* **1997**, *276*, 812–816.

(44) Michel, H.; Deisenhofer, J. *Biochemistry* **1988**, *27*, 1–7.

(45) Thompson, M. A.; Zerner, M. C. *J. Am. Chem. Soc.* **1991**, *113*, 8210–8215.

(46) Marchi, M.; Gehlen, J. N.; Chandler, D.; Newton, M. *J. Am. Chem. Soc.* **1993**, *115*, 4178–4190.

(47) Napier, G. D. R.; Neilson, J. D.; Shepherd, T. M. *Chem. Phys. Lett.* **1975**, *31*, 328–330.

(48) Sager, W. F.; Filipesc., N; Serafin, F. A. *J. Phys. Chem.* **1965**, *69*, 1092–&.

(49) Filipescu, N.; Sager, W. F.; Serafin, F. A. *J. Phys. Chem.* **1964**, *68*, 3324–&.

(50) Mishra, K. C.; Berkowitz, J. K.; Johnson, K. H.; Schmidt, P. C. *Phys. Rev. B* **1992**, *45*, 10902–10906.

(51) Fernandes, J. A.; Ferreira, R. A. S.; Pillinger, M.; Carlos, L. D.; Goncalves, I. S.; Ribeiro-Claro, P. J. A. *Eur. J. Inorg. Chem.* **2004**, 3913–3919.

(52) Mita, Y.; Togashi, M.; Yamamoto, H. *J. Lumin.* **2000**, *87—89*, 1026–1028.

(53) Lis, S.; Elbanowski, M.; Makowska, B.; Hnatejko, Z. *J. Photochem. Photobiol. A* **2002**, *150*, 233–247.

(54) Tallant, D. R.; Seager, C. H.; Simpson, R. L. *J. Appl. Phys.* **2002**, *91*, 4053–4064.

(55) Kutsenko, A. B.; Heber, J.; Kapphan, S. E.; Demirbilek, R.; Zakharchenya, R. I. *Phys. Status Solidi C* **2005**, *2*, 685–688.

(56) Fu, L. M.; Ai, X. C.; Li, M. Y.; Wen, X. F.; Hao, R.; Wu, Y. S.; Wang, Y.; Zhang, J. P. *J. Phys. Chem. A.* **2010**, *114*, 4494–4500.

(57) Sato, S.; Wada, M. *Bull. Chem. Soc. Jpn.* **1970**, *43*, 1955–1962.

(58) de Sa, G. F.; Malta, O. L.; Donega, C. D.; Simas, A. M.; Longo, R. L.; Santa-Cruz, P. A.; da Silva, E. F. *Coord. Chem. Rev.* **2000**, *196*, 165–195.

(59) Crosby, G. A.; Alire, R. M.; Whan, R. E. *J. Chem. Phys.* **1961**, *34*, 743–&.

(60) Zhang, H.; Song, H. W.; Yu, H. Q.; Bai, X.; Li, S. W.; Pan, G. H.; Dai, Q. L.; Wang, T.; Li, W. L.; Lu, S. Z.; Ren, X. G.; Zhao, H. F. *J. Phys. Chem. C* **2007**, *111*, 6524–6527.

(61) Gerbec, J. A.; Magana, D.; Washington, A.; Strouse, G. F. *J. Am. Chem. Soc.* **2005**, *127*, 15791–15800.

(62) Washington, A. L.; Strouse, G. F. *Chem. Mater.* **2009**, *21*, 3586–3592.

(63) Washington, A. L.; Strouse, G. F. *J. Am. Chem. Soc.* **2008**, *130*, 8916–8922.

(64) Lovingood, D. D.; Oyler, R. E.; Strouse, G. F. *J. Am. Chem. Soc.* **2008**, *130*, 17004–17011.

(65) Berman, S. M.In *Publications of the Lighting Research Group*; Lawrence Berkeley Laboratory: Berkeley, CA, 1995.

(66) Bourhill, G.; Palsson, L. O.; Samuel, I. D. W.; Sage, I. C.; Oswald, I. D. H.; Duignan, J. P. *Chem. Phys. Lett.* **2001**, *336*, 234–241.

(67) McCamy, C. S. *Color Res. Appl.* **1992**, *17*, 142–144.

(68) Peng, X. G.; Manna, L.; Yang, W. D.; Wickham, J.; Scher, E.; Kadavanich, A.; Alivisatos, A. P. *Nature* **2000**, *404*, 59–61.

(69) Panda, A. B.; Glaspell, G.; El-Shall, M. S. *J. Phys. Chem. C* **2007**, *111*, 1861–1864.

(70) Alarcon-Flores, G.; Aguilar-Frutis, M.; Garcia-Hipolito, M.; Guzman-Mendoza, J.; Canseco, M. A.; Falcony, C. *J. Mat. Sci.* **2008**, *43*, 3582–3588.

(71) Nakamoto, K. *Infrared and Raman Spectra of Inorganic and Coordination Compounds, Applications in Coordination, Organometallic, and Bioinorganic Chemistry*; Wiley: Hoboken, NJ, 2009.

(72) Meulenberg, R. W.; Strouse, G. F. *J. Phys. Chem. B* **2001**, *105*, 7438–7445.

(73) Binnemans, K. *Rare-Earth Beta-Diketonates*; Elsevier: Amsterdam, 2005; Vol. 35, Chapter 25.

(74) Scolan, E.; Sanchez, C. *Chem. Mater.* **1998**, *10*, 3217–3223.

(75) Berrettini, M. G.; Braun, G.; Hu, J. G.; Strouse, G. F. *J. Am. Chem. Soc.* **2004**, *126*, 7063–7070.

(76) Hartmann, S. R.; Hahn, E. L. *Phys. Rev.* **1962**, *128*, 2042–2053.

(77) Garnweitner, G.; Hentschel, J.; Antonietti, M.; Niederberger, M. *Chem. Mater.* **2005**, *17*, 4594–4599.

(78) Guo, H.; Zhang, W.; Lou, L.; Brioude, A.; Mugnier, J. *Thin Solid Films* **2004**, *458*, 274–280.

(79) Bordun, O. M.; Bordun, I. M. *Ukr. Fiz. Zh.* **1998**, *43*, 275–278.

(80) Osipov, V. V.; Rasuleva, A. V.; Solomonov, V. I. *Opt. Spectrosc.* **2008**, *105*, 524–530.

(81) Bordun, O. M. *J. Appl. Spectrosc.* **2001**.

(82) Meyssamy, H.; Riwotzki, K.; Kornowski, A.; Naused, S.; Haase, M. *Adv. Mater.* **1999**, *11*, 840–844.

(83) Wakefield, G.; Holland, E.; Dobson, P. J.; Hutchison, J. L. *Adv. Mater.* **2001**, *13*, 1557–1560.

(84) Dai, Q. L.; Song, H. W.; Bai, X.; Pan, G. H.; Lu, S. Z.; Wang, T.; Ren, X. G.; Zhao, H. F. *J. Phys. Chem. C* **2007**, *111*, 7586–7592.

(85) Famengo, A.; Anantharaman, S.; Ischia, G.; Causin, V.; Natile, M. M.; Maccato, C.; Tondello, E.; Bertagnolli, H.; Gross, S. *Eur. J. Inorg. Chem.* **2009**, 5017–5028.

(86) Pinna, N.; Garnweitner, G.; Antonietti, M.; Niederberger, M. *J. Am. Chem. Soc.* **2005**, *127*, 5608–5612.

(87) Nelson, J. A.; Brant, E. L.; Wagner, M. J. *Chem. Mater.* **2003**, *15*, 688–693.

(88) Fauteux, C.; Longtin, R.; Pegna, J.; Therriault, D. *Inorg. Chem.* **2007**, *46*, 11036–11047.

(89) Xu, L.; Hu, Y. L.; Pelligra, C.; Chen, C. H.; Jin, L.; Huang, H.; Sithambaram, S.; Aindow, M.; Joesten, R.; Suib, S. L. *Chem. Mater.* **2009**, *21*, 2875–2885.